Materials and Design 136 (2017) 137–149

Contents lists available at ScienceDirect

Materials and Design

journal homepage: www.elsevier.com/locate/matdes

Direct observation of void evolution during cement hydration

Masoud Moradian [a,*], Qinang Hu [a], Mohammed Aboustait [a], M. Tyler Ley [a], Jay C. Hanan [b], Xianghui Xiao [c], George W. Scherer [d], Zhidong Zhang [d]

[a] Oklahoma State University, School of Civil and Environmental Engineering, Stillwater, OK 74078, USA
[b] Oklahoma State University, School of Mechanical and Aerospace Engineering, Tulsa, OK 74106, USA
[c] Argonne National Laboratory, Advanced Photon Source, Argonne, IL 60439, USA
[d] Princeton University, Department of Civil & Environmental Engineering, Princeton, NJ 08544, USA

HIGHLIGHTS

- A novel in-situ technique is used for direct observation of air-filled space formation in cement paste microstructure.
- Air-filled voids are observed to increase in volume and then decrease and stay constant.
- The void size distribution changes from a few coarse voids to a large number of small and uniformly distributed voids.
- It is suggested that the air-filled void changes are caused by exsolution.

GRAPHICAL ABSTRACT

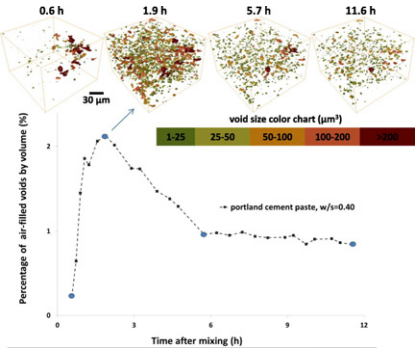

ARTICLE INFO

Article history:
Received 7 June 2017
Received in revised form 28 August 2017
Accepted 26 September 2017
Available online 28 September 2017

Keywords:
X-ray computed tomography
Cement hydration
Void evolution
Calorimetry
Induction period
Exsolution

ABSTRACT

This paper follows the hydration of both portland cement and tricalcium silicate pastes between 30 min and 16 h of hydration. In-situ fast X-ray computed tomography (fCT) was used to make direct observations of the air-filled void formation in w/s of 0.40 to 0.70 with a micron resolution.
The results show that over the first hour of the acceleration period the volume of air-filled voids reaches a maximum value and then decreases during the acceleration period and stays constant. The void distribution changes from a few coarse voids to a large number of smaller and more uniformly distributed voids. This behavior is suggested to be controlled by changes in the ionic strength that cause exsolution of dissolved air from the pore solution.

1. Introduction

The hydration of cement paste has received significant attention because the ultimate mechanical properties and durability of hardened concrete are controlled by the microstructure development [1–3]. Specifically, the porosity of cementitious paste directly impacts the mechanical properties, durability, and dimensional stability of concrete [1,4–6]. Therefore, a better understanding of pore system development and the influencing parameters are of great importance.

Most conventional methods of measuring porosity, such as mercury intrusion porosimetry, sorptivity, gas adsorption, helium inflow, acoustic emission, and alternating current impedance spectroscopy, are

* Corresponding author.
E-mail address: masoud.moradian@okstate.edu (M. Moradian).

https://doi.org/10.1016/j.matdes.2017.09.056
0264-1275/

useful to provide information about the total pore content and give insights into the bulk void size distribution [7–13]. However, these techniques cannot resolve details of the shape, size or spatial distribution of the voids. Moreover, most of these techniques cannot investigate the in-situ development and formation of pores at early ages without disturbing the sample. In recent decades, imaging techniques such as scanning electron microscopy (SEM) and transmission electron microscopy (TEM) are widely used to investigate the microstructure and pores at various ages in cement paste [14–17]. Although SEM and TEM provide images with high resolution, the results are limited to the investigated 2D cross-section of the sample [18]. In addition, the required sample preparation, such as drying and polishing, may cause artifacts in fragile samples.

X-ray computed tomography (XCT) is a powerful and non-destructive technique that can be completed in many cases with no sample preparation [17,19–25]. This method has been used in numerous studies to identify the engineering properties of a cementitious system such as aggregate spatial distribution [26], transport properties [27,28], determination of air void parameters [26, 29–32], and to examine leaching [21]. This equipment is also widely used in medicine to look at biological samples non-destructively [33, 34]. The methods used are the same, only at different length scales. A series of 2D X-ray radiographs are acquired from different viewing angles and the data are used to build a 3D rendering of the sample. The 3D rendering can be used for morphological and quantitative analyses. The gray value in the produced images is a function of X-ray absorption and can indicate differences in chemistry and density of the materials [19,23,35]. The contrast in gray value intensities can be used to evaluate an XCT dataset quantitatively by separating the collected images into regions of different constituents. This process is called segmentation.

In spite of the powerful abilities of ordinary XCT, the necessary time for data acquisition at a micron length scale may be several hours and so it cannot be used to study rapidly evolving processes, such as what occurs during the first hours of hydration of cementitious paste [36–38]. Measurements show that the Ca concentration continuously increases over the first hours of hydration reaching a maximum at the end of the induction period and then decreasing [39–41]. These ionic concentration changes have been linked to changes in the microstructure and are important in hydration [2,24,41–43]. It is also important to note that previous experiments using acoustic emission have detected signals that were interpreted as void formation during the solidification of cement paste at early ages [13]. The acoustic emission technique is a bulk measurement, so it is not able to give a detailed description of the void formation.

To study cement hydration at early ages, some researchers have collected tomographs from the first hours of hydration by lowering the exposure time and number of acquired projections [36,44]. However, the results have significant artifacts and limited contrast. Consequently, previous XCT studies on porosity have focused on systems after initial set and have observed porosity decrease from infilling of hydration products [18,19,36].

Recent breakthroughs in X-ray imaging now enable tomography data collection to be made at near video acquisition rates at the Advanced Photon Source (APS) at Argonne National Laboratory. The technique is named fast computed tomography (fCT). This advancement is possible because of improvements in detectors, precision stages, and increased photon flux [38,45–47]. While this technique has been used to study many dynamic processes, there are few published works that have used fCT to investigate cement hydration [24,36,48,49].

This study used fCT to investigate the air-filled void system evolution in cementitious pastes with industrially relevant w/s during the first 16 h of hydration. The data provide important insights about the void formation and can be useful to verify analytical models and improve their assumptions about mass transport.

2. Materials and methods

2.1. Materials

Two cementitious materials were used in this study, portland cement 168 (hereafter termed OPC) from the Proficiency Sampling Program of the Cement and Concrete Reference Laboratory (Frederick, Maryland) and monoclinic tricalcium silicate powder (mC_3S)[1] from Mineral Research Processing (Meyzieu, France). These powders were characterized by ASTM C114 testing method and X-ray diffraction (XRD) for chemical analysis of OPC; automated scanning electron microscopy (ASEM) was used for particle size distribution and chemical analysis of mC_3S.

The results of the chemical composition analysis, Blaine fineness (ASTM C204), and density measurements are presented in Table 1. XRD analysis showed that mC_3S is close to pure C_3S. XRD analysis of OPC is available in another publication [50]. The details of the ASEM technique and the particle size distribution of both powders can be found in the appendix. Based on the Blaine fineness and particle size distributions, OPC is finer than mC_3S.

2.2. Sample preparation

The mixing procedure was the same for all samples examined by fCT, isothermal calorimetry, or chemical shrinkage. First, water was added to 5 g of the powder. After adding the water, the mixture was stirred by a stainless steel rod ten times clockwise and then ten times counterclockwise in a glass vial. Then the vial was shaken by a vortex mixer (produced by Stuart-Staffordshire, UK) with a speed of 1000 rpm for 3 min. After mixing, a 1.5 mm diameter by 6 mm length polyethylene tube was pushed into the fresh paste. The tube was inserted to capture about 4 mm of paste. A finger was then used to cover the end of the tube and it was removed from the fresh paste. The vacuum generated in the sealed tube held the fresh paste within the tube as it was removed. The tube was then sealed with clay to minimize vapor transport and loss of mixing water during scanning. Finally, the sample was compacted by holding the sealed sample in one hand and clapping it into other hand ten times.

Five paste samples were produced for examination and the details of the tests are presented in Table 2. Four paste samples were produced with deionized water as a mixing liquid, while the fifth sample was made with OPC and de-aired water with w/s = 0.60. The deionized water was produced first by reverse osmosis and then treated with an ASTM D5127 Type 1 ultra-pure water system. During this process the water was pressured to approximately 4 bar.

To produce the de-aired water, the deionized water was boiled and then cooled to room temperature in a He environment. Helium was used because of its low solubility in water [51]. While still in the He environment the de-aired water was added to the OPC powder by a syringe and then mixed as per the standard procedure.

The first tomograph was acquired after sample preparation and alignment of the instrument. This took 34 min to 70 min for each sample.

2.3. Isothermal calorimetry and chemical shrinkage

Isothermal calorimetry was used to measure the heat of hydration. This test was conducted with a Tam Air Isothermal Calorimeter on samples at a constant temperature of 25 °C over 18 h. The heat capacity of OPC and mC_3S was 0.753 $Jg^{-1}\ K^{-1}$, and the capacity of deionized water was 4.1814 $Jg^{-1}\ K^{-1}$ [52]. The samples were made in the same way as the fCT experiments, except that 3 g of powder was used. After

[1] Conventional cement chemistry notation is used throughout this paper: C = CaO, S = SiO_2, H = H_2O.

Table 1
Specifications and bulk chemical composition of cementitious materials.

	Blaine (cm^2/g)	BET surface area (m^2/g)	Density (gr/cm^3)	Chemical composition (mass %)						Phase concentration (%)			
				SiO_2	CaO	Al_2O_3	MgO	Fe_2O_3	SO_3	C_3S	C_2S	C_3A	C_4AF
OPC	4080	NA	3.15	19.91	62.27	5.11	3.87	2.15	3.49	54.5	15.7	8.0	7.0
mC_3S	3588	0.86	3.12	26.54	71.97	0.94	0.06	0.48	–	≈100	–	–	–

mixing, the vials containing the fresh paste were capped and added to the calorimeter.

The chemical shrinkage measurements were made in the same manner as other samples in this paper but the mixture used 20 g of powder and the chemical shrinkage was measured for 18 h. In this method, a sensitive differential pressure sensor is used to measure the water level drop caused by chemical shrinkage in a capillary tube. More details can be found in other publications [53,54].

2.4. Fast X-ray computed tomography

The fCT was conducted at the 2-BM beamline at the Advanced Photon Source (APS) at Argonne National Laboratory. This technique allows collection of tomographs in <5 s. This fast data acquisition is from high speed detectors, a fast but stable rotation stage, and a high photon flux. The projections were acquired at angular increment of 0.125° over a rotation of 180°. This created 1500 radiographs to produce each tomograph. The tomographs were collected at 10 min intervals in a room with constant temperature of 25 °C. The instrument settings for the scans are provided in appendix. More details about the facilities can be found in other publications [45,46].

2.5. Reconstruction and segmentation

The 2-D radiographs were reconstructed using a Fast Fourier Transforms (FFT) algorithm [46]. The same instrument and reconstruction settings were used for all subsequent tomographs to make quantitative comparisons. Fig. 1 shows a typical data set from mC_3S with a w/s = 0.70 as well as a typical cross section and a segmented image that highlights the voids.

Each image is made up of individual pixels with a 16-bit gray value. The variation of gray value within the scanned sample is caused by the differences in the atomic electron density and/or the bulk density of the imaged material [55]. Absorption tomography is defined by the Beer-Lambert Law:

$$\frac{I}{I_o} = exp(-\mu_m x) \quad (1)$$

where I is transmitted intensity, I_o is incident intensity, μ_m is X-ray mass attenuation coefficient, and x is the length travelled by the X-rays [56].

To reduce computational efforts, 100 slices out of 1500 were analyzed from each data set. Moreover, the inner section of the sample was investigated to avoid edge effects. This space contained roughly 60,000 anhydrous particles to be imaged in each tomograph [24]. To reduce noise in the data, a median filter with a radius of 2.5 μm was applied to all slices. This filter is used to preserve image edges with minimal signal distortion. It has been widely used by others [57,58].

Table 2
Details of fCT paste samples.

Cementitious material	w/s	Water type	Time for first tomograph (min)	Time for last tomograph (h: min)
mC_3S	0.70	Deionized	70	15:40
mC_3S	0.45	Deionized	70	15:40
OPC	0.60	Deionized	34	11:34
OPC	0.40	Deionized	34	11:34
OPC	0.60	De-aired	43	9:47

While there are many possible segmentation algorithms, one common method is to use a single gray value that separates a target material in the images. This study aims to track the evolution of air-filled voids. This means that the method needs to be used to track how the air-filled voids changed in comparison to the rest of the paste. To determine which gray value should be used to separate air-filled space in each sample, at least 30 individual air-filled voids from various locations in the region of interest (ROI) and from different time periods were identified by an operator and the average gray value of each one was determined. This process was repeated for each sample to find the average gray value of voids for that specific sample. A histogram of the measured data on OPC w/s = 0.60 can be found in the appendix.

The gray values within voids were found to be normally distributed. This means that 99.7% of the expected values are contained within three standard deviations of the mean and so this value was used for the void segmentation. This provided an easy approach that could be applied for each investigated sample while still providing a high level of confidence in the data. Fig. 1 shows a region of a slice obtained from mC_3S with w/s = 0.70 before and after the segmentation of air-filled voids. More details of the reconstruction and image processing can be found in the appendix.

2.6. Measuring void spacing

The uniformity of void distribution is quantified by estimating the average nearest-neighbor distance between individual voids at different time periods. This was investigated by measuring center-to-center nearest-neighbor distance for each individual void within each tomograph corresponding to a specific time period. Then, the average and standard error of all measured distances are calculated in the tomograph and reported as the average nearest-neighbor distance of voids in the sample at the corresponding time period.

3. Results and discussion

3.1. Isothermal calorimetry and chemical shrinkage

Fig. 2 demonstrates the heat flow results of four pastes over the 18 h of hydration. The results of the OPC samples are shown by black lines, while gray is used for mC_3S. This same nomenclature is used throughout the paper. The w/s was chosen to match the values used in the fCT experiments. The OPC system showed a higher heat release compared to the mC_3S system. This difference may be attributed to the different chemical composition, w/s, and particle size distribution of the examined powders.

The chemical shrinkage curves for four OPC or mC_3S samples are shown in Fig. 3. This figure shows that chemical shrinkage follows almost the same curve for at least 18 h independent of w/s. The samples with a lower w/s have a higher amount of chemical shrinkage.

3.2. Volume change of air-filled voids and heat of hydration

Fig. 4 demonstrates the changes in total volume of the air-filled voids measured by fCT over the first 16 h of hydration. Each point in the graph represents the volume percentage of the air-filled voids at each time period.

For all of the samples investigated the air content increases and then decreases to a constant value. While the results for the mC_3S

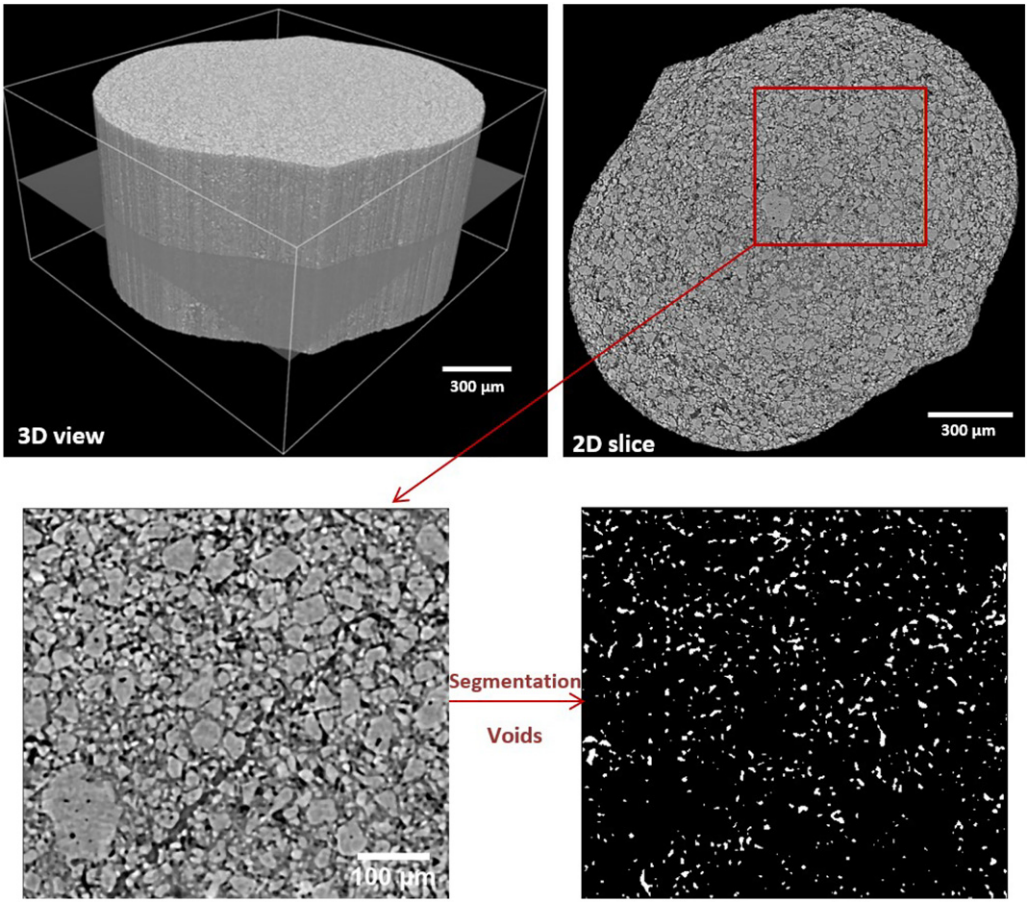

Fig. 1. Typical data sets from fCT of the 3D reconstruction and region of interest. The result of the segmentation for the air filled space is shown for mC_3S paste with w/s = 0.70.

with a w/s = 0.45 appear to be different, it is probably that a peak has occurred before the first collected tomograph at 70 min. The samples made with lower w/s seem to have reached their peak earlier than those with a higher w/s. The behavior of individual voids is also investigated; it is found that the volume change of the single voids follows a similar trend to that of the overall system; however, they have some differences based on their size. More details can be found in the appendix.

The sample with de-aired water had the lowest measured volume of air and showed minimal volume change during the time investigated. It is expected that some air-filled space would be trapped during mixing and there may be only a slight increase in the observed volume. This suggests the de-aired water is important to the mechanism causing the void volume increase. This will be discussed in more detail later in the paper.

Fig. 5 combines the volume change of the air-filled voids for the samples that did not use de-aired water with the isothermal calorimetry curves. The total volume of air-filled voids is increasing during the induction period. The peak void volume seems to occur within the

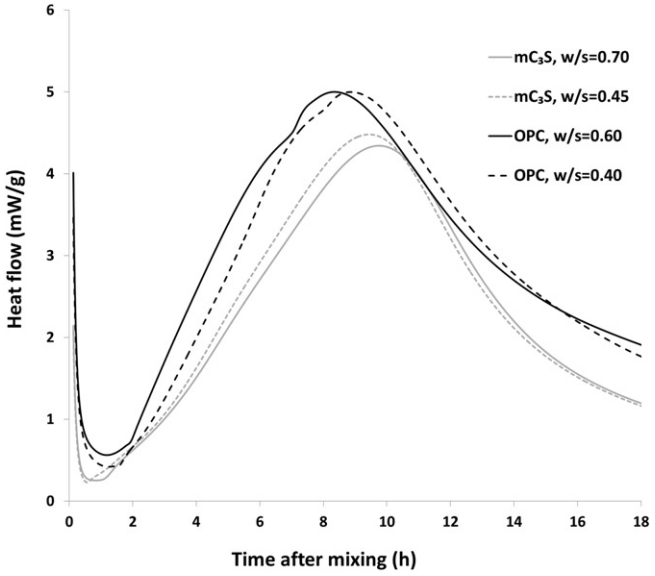

Fig. 2. Heat evolution curve of the pastes made with deionized water.

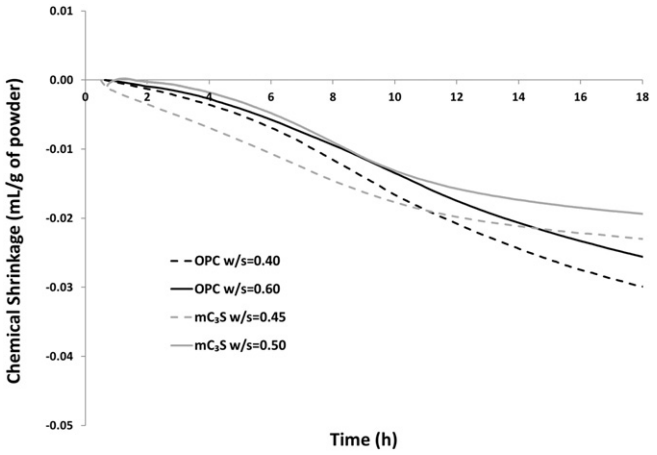

Fig. 3. Chemical shrinkage of the pastes made with deionized water.

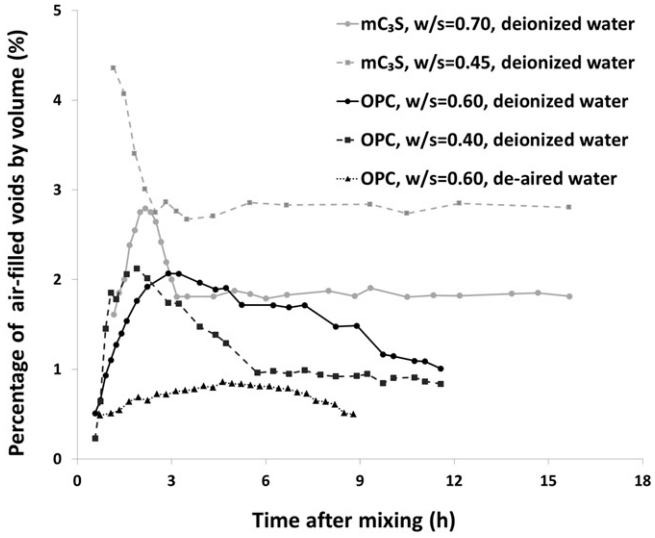

Fig. 4. Volume change of air-filled voids over time.

first hour of the acceleration period. Later, the total volume of voids apparently decreases during the acceleration period. Finally, the bulk volume stays constant after ≈3 h for mC_3S samples and 6 h for OPC w/s = 0.40, which may be caused by initial set; there is slight downward drift for OPC with w/s = 0.60 after about 7 h.

3.3. Spatial distribution of voids

The evolution of voids in OPC w/s = 0.40 and mC_3S w/s = 0.70 is shown in 3D and with representative 2D slices in Figs. 6 and 7. The raw data from a 2D slice are shown at the left with the segmented image in the middle showing the air-filled voids as a binary image. The 3D renderings are shown on the right where the volumes of the voids are shown with different colors. The voids larger than 200 μm^3 are shown in red and those smaller than 25 μm^3 are green. Other sizes are shown by colors between red and green and details can be found in the legend.

These images help the reader to visualize the results and make general observations. Similar observations are made for both mC_3S and OPC at different w/s and so the observations will be jointly discussed. More quantitative data will be given later in the paper. Both images show that voids smaller than ≈100 μm^3 are forming between 0.6 h and 2.5 h, while the larger voids are observed to decrease in size.

It also appears that the spatial distribution of the voids changes over time. Fig. 8 shows the change in the average nearest-neighbor distance between individual voids in different time periods of the experiments. Each point in the graph is an average of the calculated nearest-

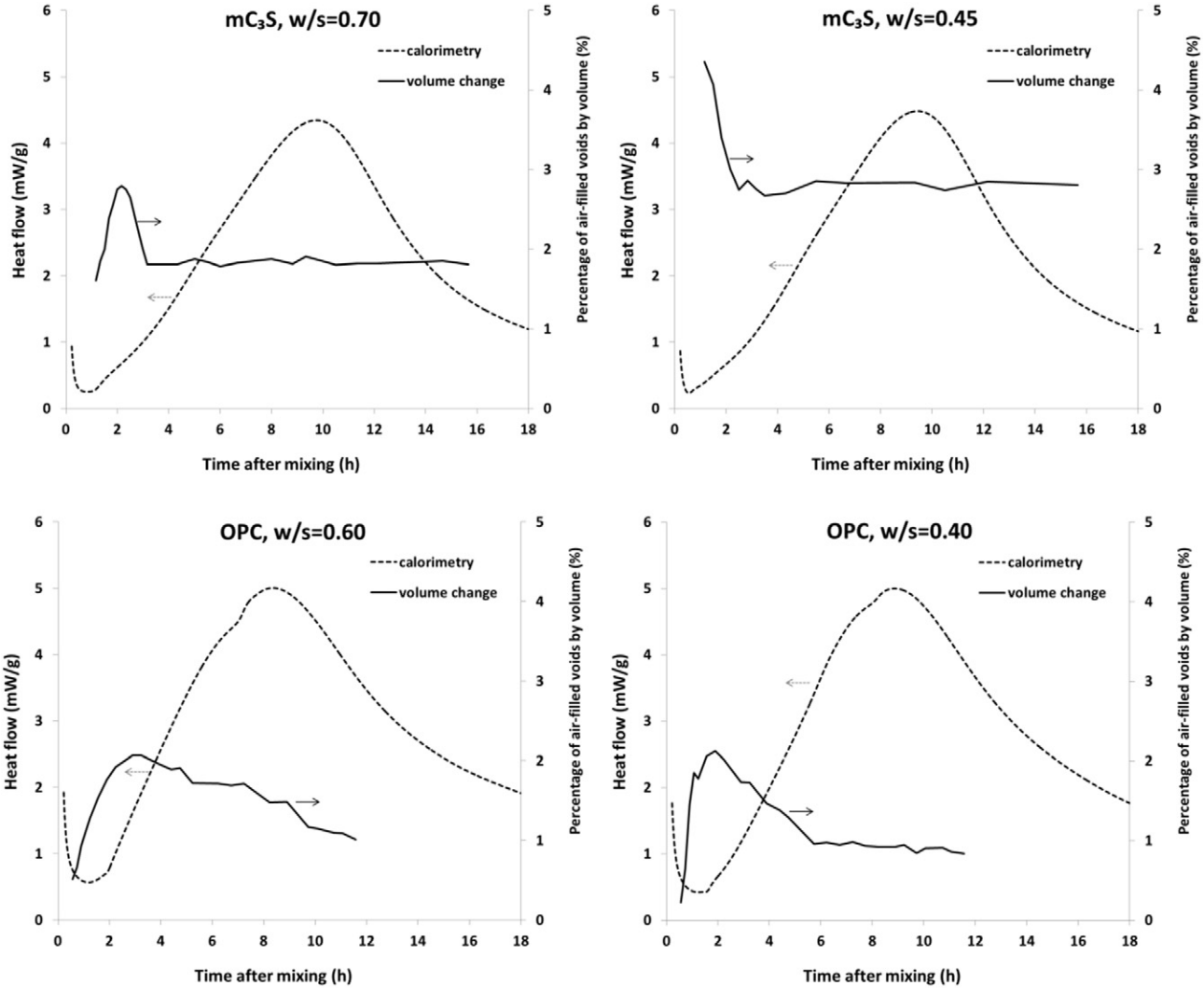

Fig. 5. Comparison of heat release to volume change of air-filled voids in samples made with deionized (not de-aired) water.

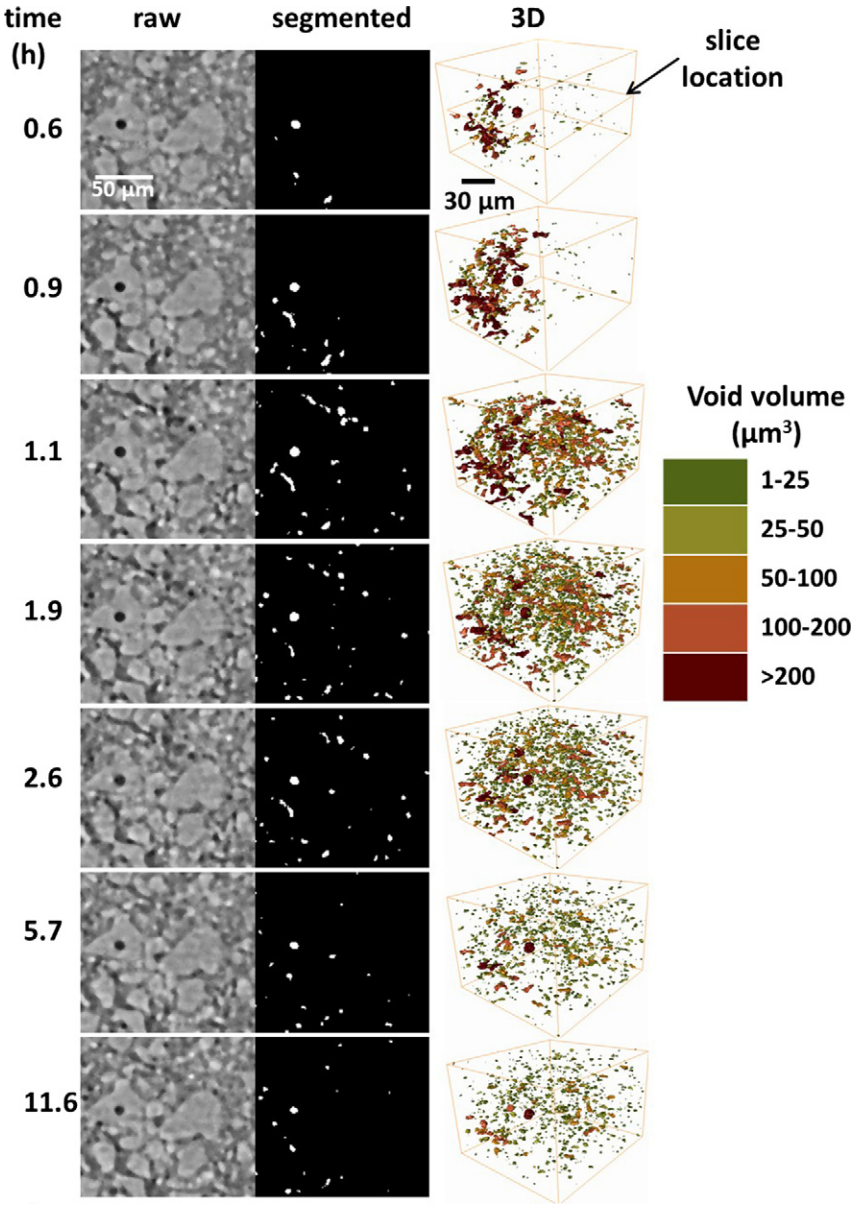

Fig. 6. 3D view of void size distribution in critical time periods of OPC w/s = 0.40.

neighbor distance for all individual voids in the corresponding time period. One standard error is also reported.

The average distance between voids in samples made with deionized water is higher before ≈2.5 h, which is during the induction period. Over time, the average distance for all samples reaches a constant value, such that the spatial distribution of the voids is almost constant after ≈4 h. This supports the observations from the 3D views that shows almost constant void spacing after 3 h as shown in Figs. 6 and 7.

The distance between voids in the sample made with de-aired water was significantly higher than the other samples. This was expected since this sample has the lowest amount of air-filled voids. As a result, the number of voids should be lower and therefore their spacing is higher. If the void formation is caused by exsolution of dissolved gas in the liquid, then the nucleation location and frequency will be dependent on the ionic concentration of the liquid. This will be discussed in the next sections.

3.4. Change in size distribution

Further insights can be gained by observing the change in the total volume percentage over time for voids of different volumes as shown in Fig. 9. These graphs have been normalized to the total volume of voids in the sample in the specific time periods. Over time the volume percentage of small voids increases while the volume percentage of the larger voids decreases. Arrows have been added to Fig. 9 to highlight this. For example, after 1.2 h of hydration, the mC_3S paste with w/s = 0.70 had about 18% of the total void volume contained in voids larger than 1000 μm^3. For this same sample only 2% of the volume was found in these voids after 15.7 h. Conversely, after 1.2 h about 9% of total void volume was contained in voids with a volume <15 μm^3. After 15.7 h this increased to 17%. Since these voids are so small this would indicate a significant increase in the number of voids. The formation of these <20 μm^3 voids can be observed in Fig. 6 and Fig. 7. Similar behavior is observed in all of the samples made with deionized water. In contrast, negligible change has occurred in voids smaller than 100 μm^3 in the sample made by de-aired water, while the percentage of voids larger than 1000 μm^3 decreases from 37.5% at 0.7 h to 9.2% after 8.8 h. This is likely caused by the infilling of the hydration products over this time period.

The voids between 100 and 200 μm^3 do not change substantially for samples made with deionized water except OPC w/s = 0.40, which has

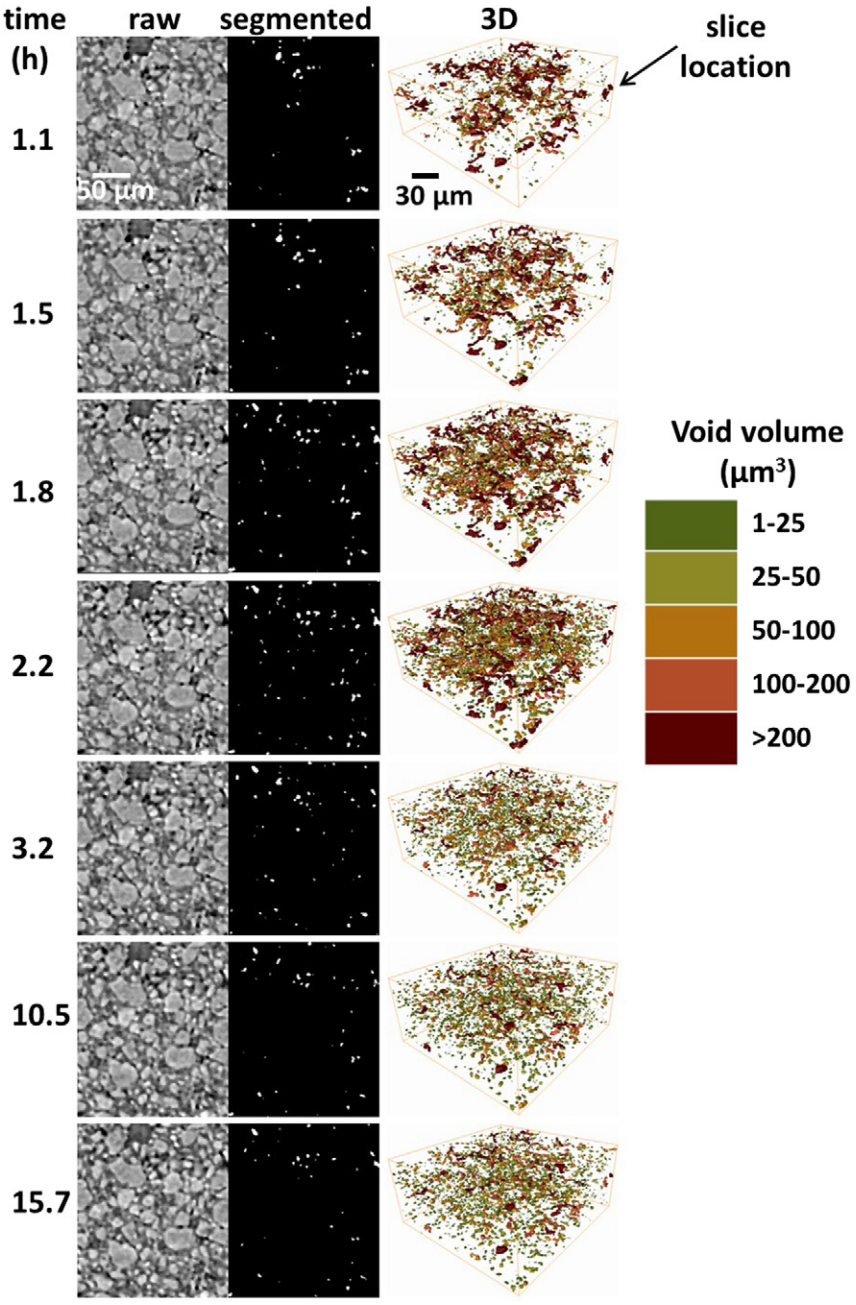

Fig. 7. 3D view of void size distribution in critical time periods of mC_3S w/s = 0.70.

a finer void distribution before 2.5 h compared to the other samples. This could be caused by the lower w/s.

The change in size distribution of samples made with deionized water is considerable over the first 2.5 h of hydration. However, the size distribution becomes stable during the acceleration period and then shows little change afterward. This matches the total volume changes observed in Fig. 4 and Fig. 5.

Movies that combine Figs. 4,5,6,7, and 9 on the same display are shared in the Supplementary files. Readers are encouraged to watch these to better appreciate the complex shifts in the distribution.

3.5. Comparison of size distribution change over time

Fig. 10 compares the data in Fig. 9 at the same time periods. The samples made with deionized water were significantly different than the sample with de-aired mixing water. At 1.2 h of hydration, three of the samples have very similar void size distribution; however, the OPC with w/s = 0.40 has 33% of the void volume larger than 100 μm^3. The other three samples made with deionized water have almost double this. This might be caused by the closer spacing of the cement particles from the lower w/s, different compaction level, and the higher chemical reactivity of OPC compared to mC_3S. More observations are needed to better understand this.

At 2.5 h, the amount of air-filled voids larger than 100 μm^3 decreased in all samples. Since the OPC with w/s = 0.40 started with a lower amount of voids > 100 μm^3, the decrease in these voids caused this sample to have only 21% voids > 100 μm^3. The other samples made with deionized water had between 43%–48% of their voids larger than 100 μm^3. As mentioned earlier, the sample made with de-aired water is different than others and 92% of air-filled voids are > 100 μm^3. While this sample has the lowest volume of air-filled voids, the voids > 100 μm^3 constitute > 90% of the air-filled space at 1.2 h and 2.5 h.

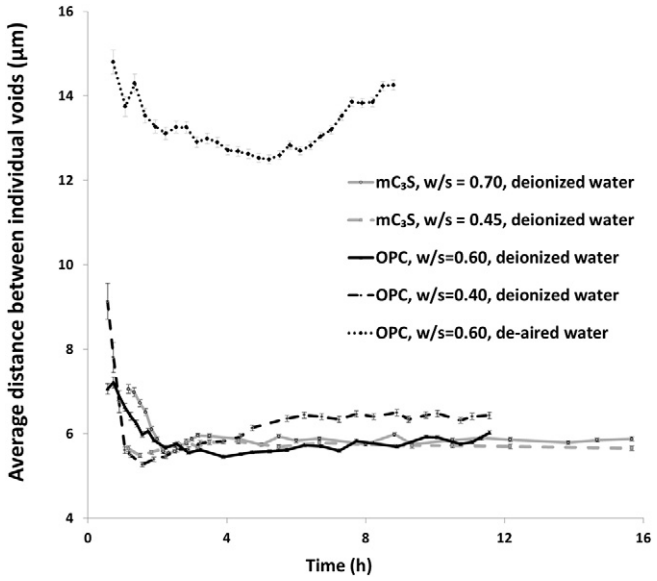

Fig. 8. Average nearest-neighbor distance between air-filled voids in different time periods.

After 4.8 h and 9 h of hydration in samples made with deionized water, the samples with similar w/s showed similar size distributions regardless of whether the paste was mC_3S or OPC. The samples with a higher w/s were found to have a lower amount of smaller voids and a higher amount of the larger voids after 9 h. For mC_3S with w/s = 0.70 and OPC with w/s = 0.60 between 60% to 64% of voids are smaller than 100 μm^3 and for the OPC with w/s = 0.40 and mC_3S with w/s = 0.45 over 82% of voids are smaller than 100 μm^3 after 4.8 h. These size ranges did not greatly change from 4.8 h to 9 h.

The samples with a w/s of 0.60 and 0.70 had between 27% to 34% voids >100 μm^3 while the samples with w/s of 0.40 and 0.45 has <11% of the voids in this size range. In contrast, the sample with de-aired water has over 89% and 80% of the air-filled voids >100 μm^3 after 4.8 h and 9 h, respectively. This highlights the importance of dissolved air on the microstructural evolution of portland cement systems. These mechanisms will be discussed further in this paper.

3.6. Discussion of findings

The trends in volume change shown in Fig. 4 are similar for all samples made with different materials and w/s except for the sample using de-aired water. In addition, the changes observed in the first 3 h of hydration are much greater than the variation in the constant portion of the curves observed after 3 h.

The sensitivity of the results to the segmenting value is examined by altering the threshold value by ±5% for mC_3S with w/s = 0.70. The difference was selected as it was a reasonable range of variation greater than the variability in the segmentation method. The results are demonstrated in Fig. 11. The results show that while the different threshold values modify the magnitudes of curves, the variation in threshold does not change the general trend or timing of the curves. Therefore, the calculated thresholds seem to be reliable for comparing the different samples and investigating the general behavior in this study.

All tests were conducted in an environment with constant temperature and pressure. Because each scan was only 5 s in length, this means that each sample was only exposed to the X-ray radiation for roughly 7.5 min over roughly 15 h, so the damage from X-ray radiation is expected to be negligible. This is supported by other work done with the same instrument to investigate inorganic materials [59]. In addition, the samples were all prepared in the same way, but the initial investigation was not done at the same time and the samples were investigated for different lengths of time. Despite these differences, the same trends were observed in all of the experiments and the void size distribution in Fig. 11 was found to be quite comparable at similar time periods. This is not likely a coincidence. Finally, other research has inferred void formation during this time period through acoustic emission measurements [13]. The sum of this evidence suggests that the observations in this study are repeatable and not caused by beam artifacts.

4. Proposed mechanisms

The measurements show that the total volume of air-filled voids in samples made with deionized water increases continuously during the induction period, reached a peak within the first hour of the acceleration period, and then decreases as the acceleration period continues. Also, during the acceleration period the voids stop changing in volume. The initial voids observed may have been trapped by the mixing and consolidation of the sample. However, the formation and evolution of the air-filled voids are likely caused by another mechanism. In this section, two mechanisms will be discussed that could explain the observed changes: chemical shrinkage and change in ionic concentration of the solution. Each will be described and then assessed in terms of their compatibility with the experimental observations.

4.1. Contributions from chemical shrinkage

Some previous works have inferred some signs of bubble formation in cement paste slurry by observing acoustic events during the early age hydration [13,60]. These studies have attributed the formation of the air bubbles to chemical shrinkage during early age hydration reactions. According to this hypothesis, water is consumed by the reactions to produce the hydration products. It is further hypothesized that the bubbles may decrease in volume over time as water from the surface enters the sample to displace the voids or the creation of the voids causes the paste to be unstable and then collapse and this causes the voids to decrease in size [60].

The total void content of samples with a lower w/s reached its maximum volume change earlier than the pastes with higher w/s as shown in Fig. 4. These observations can be explained by chemical shrinkage. As w/s decreases, it is expected that the paste would shrink more and so a higher amount of air-filled void is formed in a shorter time period [5,6,13]. The finer size distribution of voids in the low w/s samples may be attributed to the shorter initial inter-particle distance in these paste samples. However, there is minimal chemical shrinkage observed during the times when the void formation in the fCT data is the highest. Also, this hypothesis is unable to explain why the void volume change does not continue when the chemical shrinkage is higher at the later ages. For example, Fig. 3 shows that the total chemical shrinkage after 2.5 h is only between 0.0013 mL/g and 0.0111 mL/g but the fCT shows the highest rate of change in void volume in this same period. Moreover, the chemical shrinkage value reaches between 0.0136 mL/g and 0.028 mL/g after 10 h and the fCT shows negligible void change. Because of this, it is not likely that this could be a major cause of the air volume change that is observed.

4.2. Contributions from change in ionic strength

An alternative hypothesis is the destabilization of dissolved air within the pore solution caused by an increase in the ionic strength. Water typically contains around 30 mg/L of dissolved air and the amount of air can be higher in water that has been pressurized [61–64]. The solubility of air in water depends on the temperature, pressure, and dissolved ions of the water [65,66]. For all samples, including the one made with de-aired water, the temperature and pressure of the testing environment were constant. Since the X-ray exposure was only 5 s per scan every 10 min it should have minimum impact on the sample temperature.

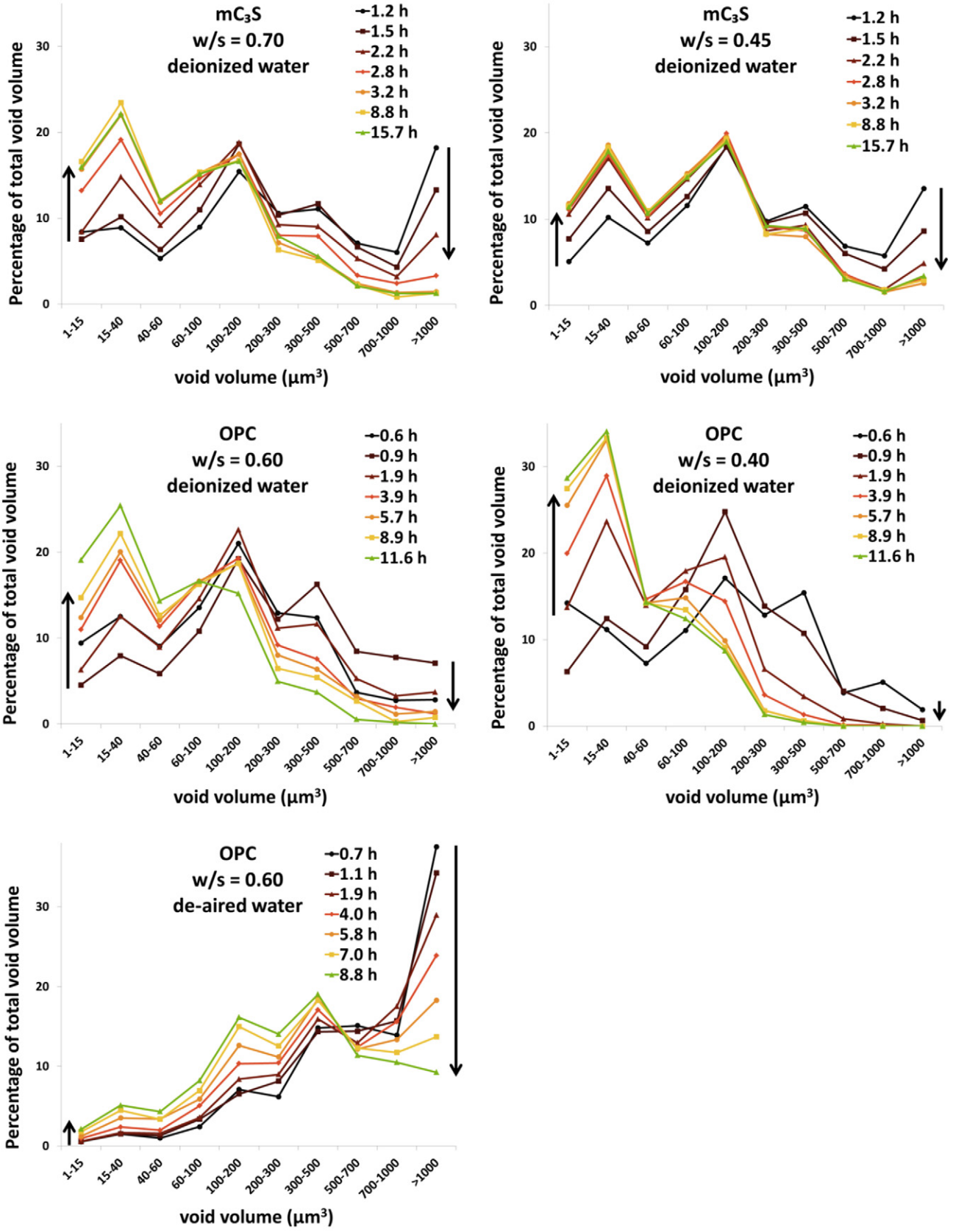

Fig. 9. Change in the air-filled void size distribution over time.

It is widely reported in the literature that the concentration of ions increases during the induction period. Dissolving cement grains will rapidly add significant amounts of ions to the solution in seconds and this will continue over time [39,40,67]. Many previous studies have shown that the Ca concentration will increase until reaching a maximum near the end of the induction period [39,40,68]. A study

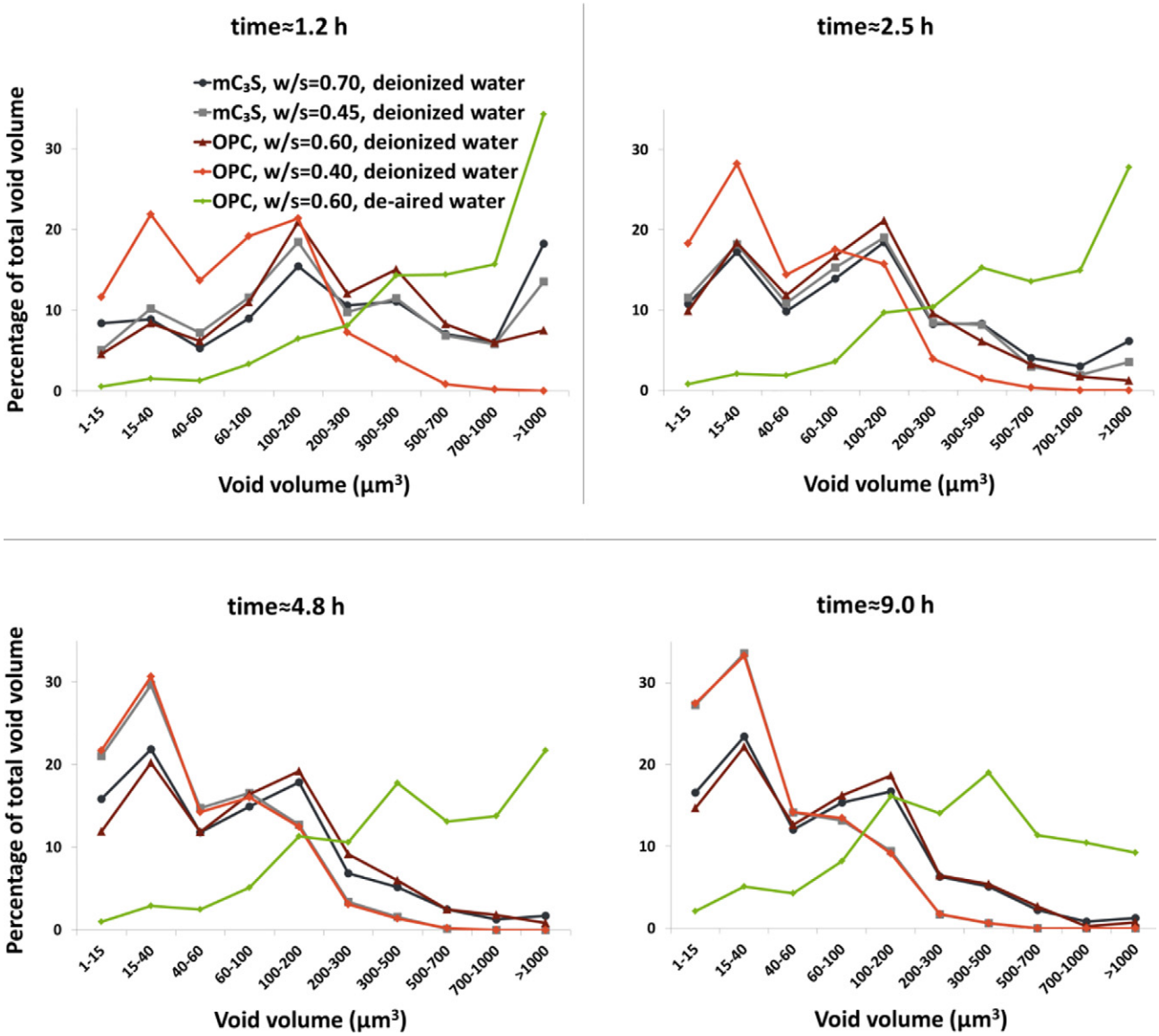

Fig. 10. Comparison of size distributions of the examined samples in different time periods.

using triclinic C_3S with a w/s = 0.70 showed the average Ca concentration of the bulk solution to be ≈1700 ppm at the end of the induction period and then drop to ≈1450 ppm as the acceleration period begins [39].

Many others have reported that air solubility decreases with an increase in the dissolved ions in the water [64,69–72]. For example, seawater has a higher propensity to produce foam than fresh water because of the higher concentration of dissolved ions [71]. In the literature, this effect is attributed to various factors including the decrease in the surface tension of the water, reduction in the hydrophobic force of attraction between bubbles, and desorption of ions from the air-water interface that ultimately destabilize the bubbles [64,69–71,73–76]. While the mechanisms are not well understood, all of the publications agree that the increase in ionic concentration of the solution causes a decrease in the solubility of the air. Therefore, it is reasonable that the dissolved air in the pore solution will become less soluble and will form gas during the induction period. The gas may join other adjacent air-filled space or it may form a new void in water filled space. Based on the size distribution changes in Fig. 9, it appears that the voids have formed in the water-filled space. This explains the continuous increase in total volume of air-filled voids over the induction period as seen in Fig. 5.

The most significant fact in support of this mechanism is that the sample made with de-aired water does not show a considerable change over time of the air-filled voids. This observation reinforces the importance of dissolved air in void formation of hydrating cement paste.

Calculations were done to estimate the volume of air that may be formed from the dissolved air. All details from the calculations can be found in the appendix. These calculations estimate the dissolved air in paste with w/s between 0.40 and 0.70, given the densities of water and cement. The deionized mixing water used in the experiments was obtained from a central water deionizer with a distribution pump. The setup resembles water delivered to a residence or a concrete plant from a distribution center. These increased pressures from distributing the deionized water will cause an increased volume of air to dissolve in solution. Residential water is typically pressurized between 200 kPa and 400 kPa [77]. The pressure of the deionized water was approximately 400 kPa. For pressures between 100 kPa and 400 kPa the dissolved air in deionized water is 20 mg/L to 120 mg/L [61–64,78]. The ionic concentration values from the literature vary between 0.25 M to 1.1 M [79–81]. If the deionized water was pressurized to 300 kPa then the volume of exsolution is estimated to be between 0.41% and 1.95% of the volume of the paste. The measured values in this work were found to be between 1.1% and 2%. This suggests that this phenomenon

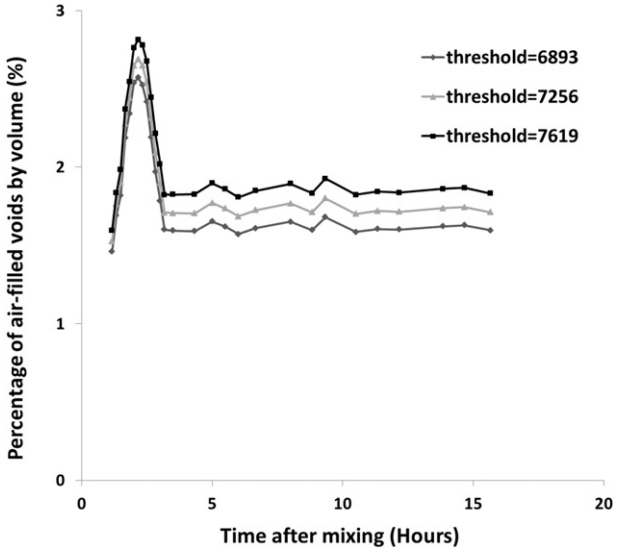

Fig. 11. Effect of different threshold gray values on the trend of the curves for mC_3S w/s = 0.70; the calculated threshold value was 7256 based on the segmentation method.

and the proposed mechanism based on the change in ionic concentration are probable.

As the acceleration period begins, the ionic concentration decreases as hydration products are precipitated [24,39,40,67,68,82]. This decrease in ionic concentration will change the solubility of the air and allow the air to dissolve. This could explain why the air leaves the bubbles and dissolves into the solution. This behavior was observed in both volume graphs and 3D images (Figs. 4, 5, 6, and 7). This volume decrease could also be caused by the formation of hydration products within the voids. Furthermore, the time lapse images in Figs. 6 and 7 show that formed voids did not change location after being formed and neither did the OPC or mC_3S solids. This means that other phenomenon such as settlement and temperature changes were not significant over the times investigated.

It is expected that air would transfer from the smaller bubbles to the larger bubbles through Ostwald ripening [83]. However, it appears that both the large and small voids start shrinking simultaneously. This is not consistent with Ostwald ripening. However, in high ionic strength solutions it becomes harder for air to transfer between the bubbles to redistribute their size. It is also reported by several researchers that many electrolytes inhibit bubble coalescence above a certain transition concentration depending on the type of solution [69–71,73–75,84–86]. This means that the average size of the air filled space is a function of the local dissolved ion content of the solution. This mechanism is explained further in other publications [76].

Observations from the present work support this. The large air-filled voids available in the first collected tomographs as shown by Figs. 6 and 7 suggest that there is more of a tendency for coalescence when the ionic concentration is low at the beginning of the tests. As the ionic concentration increases during the induction period, more bubbles are formed in the paste. The high ionic concentration may hinder coalescence of the bubbles in the slurry. These bubbles are dispersed and have a finer size distribution, because the solution concentration is not favorable for coalescence. This is shown by 3D images and size distribution graphs (Figs. 6, 7, and 10). Also, a more uniform spacing of the voids is observed in Fig. 8 after 3 h of hydration. Unlike the samples made with deionized water, over 80% of voids are $>100\ \mu m^3$ in the sample made with de-aired water, and the total volume and size distribution of voids do not change significantly over time. This lack of observed volume change in the de-aired sample is a strong observation that the dissolved air is important in the observed volume change.

Furthermore, the observed differences in samples with different w/s can be interpreted based on the change in ionic concentration. The pastes with the lower w/s can potentially contribute more ions to the solution because of the higher solid content in the solution [39]. This might be the reason that the total void content reaches its peak volume earlier than in samples with a higher w/s.

The higher ionic concentration of slurry in low w/s samples can also prevent coalescence of the voids formed in the solution [71,84–86]. Because these voids are less likely to coalesce at high ionic concentrations, they would be smaller and the number formed would be higher in samples with a lower w/s. The void volume, size distribution, and spacing stopped changing after about 3 h. This could be attributed to early stiffening or setting that occurs and may prevent change in the system.

Although this mechanism can explain most of the observations in this study, more details are needed in order to be able to model this phenomenon accurately. The reported solution concentrations in the literature are based on the average ionic concentration of the slurry. This will not be necessarily representative of the local ion concentration near the individual hydrating particles where the voids form. This makes the modeling of this phenomenon difficult. Research efforts are underway to make in-situ measurements to fulfill this need.

5. Practical importance of the findings

This study follows the evolution of the void system in OPC and mC_3S pastes with different w/s. It is widely understood that the microstructure impacts the performance of materials. These findings suggest that as the microstructure is being formed, there is also a creation of voids that are caused by dissolved air in the mixing water. These voids are likely important to the durability and mechanical properties of the concrete. This work should have broad implications as it is common to distribute water with pressures. This will in turn increase the number of voids observed in the system. These findings provide a deeper understanding of how w/s and mixing water properties influence the void system of hardened paste.

In addition, these observations reinforce the importance of changes in ionic concentration during hydration and how they may impact the volume and distribution of voids within different cement systems.

While there are still discussions about the mechanisms of increasing ionic strength on void formation [71,84–86], this technique can provide new insights into the current understanding of void formation and coalescence in other ionic solutions. This phenomenon is important for recognition of interactions in biological system, fluids, and slurries. The application may include drug design, protein crystallization, formulation science, oil recovery, food, and mineral flotation [74,76,84].

6. Conclusions

In this paper, fCT was used to study the evolution of air-filled voids in cementitious pastes within the first 16 h of hydration. The change in the total volume and size distribution of air-filled voids were investigated at a micron resolution. The following conclusions can be drawn for samples made with *deionized water*:

- The total volume of the air-filled voids continuously increased during the induction period. During the same time period, the average distance between individual voids decreased. A considerable amount of voids $<100\ \mu m^3$ were observed to form uniformly, while the larger voids decreased in size.
- The total volume of the voids started to decrease over the first hour of the acceleration period and ultimately reached a constant after approximately 4 h in most samples. In this time period, which coincides with initial setting, the spatial and size distribution of air-filled voids becomes more uniform.
- All samples regardless of w/s and whether they were OPC or mC_3S showed similar volume change and void distribution at comparable

times. However, the samples with a higher w/s had a higher portion of voids >100 μm^3.

The following conclusions can be drawn for samples made with *de-aired water*:

- A significantly lower volume of air-filled voids is observed in these samples and these voids do not significantly change in size or spacing over time.
- The size distribution of the voids in the sample with de-aired water mainly consisted of voids >100 μm^3 and over time these voids decreased in volume.
- This performance is drastically different than the samples made with the same materials and binder that contained deionized (but not de-aired) water. *This highlights the importance of dissolved air on the mechanism for the void formation.*

Mechanisms have been discussed involving chemical shrinkage and changes in ionic strength and their contribution to the formation of air-filled space. The ionic strength mechanism is consistent with the trends observed for the volume of air formed and the changes in size distribution, and provides insights into why the void formation is not observed in samples with de-aired water.

Furthermore, this study provides insights for improved understanding of void system development during hydration. It is noteworthy that the current study was limited by the resolution of the scans, and therefore only the voids greater than a few microns were considered. The method provides no insight into what occurs at the nanoscale; however, the high capillary pressure in such small voids makes their existence improbable.

Additional work is needed to investigate how other variables such as chemical and mineral admixtures can affect the void formation. This is an important area of ongoing research that has potential to improve the performance of concrete.

Acknowledgment

This work was supported by funding from Federal Highway Administration (FHWA) Exploratory Advanced Research (EAR) program award # DTFH61-12-H-00003 and funding from the United State National Science Foundation CMMI 1150404 CAREER Award. We thank our collaborators, Jeffrey Bullard (National Institute of Standards and Technology), Brad Chmelka (University of California, Santa Barbara), Andreas Lüttge and Rolf Arvidson (University of Bremen), Denise Silva and Josephine Cheung (GCP), and Larry Robert (Roberts Consulting), for their insightful advice on this work. A special thanks is also given to Narges Nourian for all of her help on with the data analysis. We also thank Bret Robertson for his help in the fCT data collection. The XRD measurements were made at GCP by Jeffrey Nicolich.

Use of the Center for Nanoscale Materials and the Advanced Photon Source, both Office of Science user facilities, was supported by the U.S. Department of Energy, Office of Science, Office of Basic Energy Sciences, under Contract No. DE-AC02-06CH11357.

Supplementary data to this article can be found online at https://doi.org/10.1016/j.matdes.2017.09.056.

References

[1] J.W. Bullard, H.M. Jennings, R.A. Livingston, A. Nonat, G.W. Scherer, J.S. Schweitzer, K.L. Scrivener, J.J. Thomas, Mechanisms of cement hydration, Cem. Concr. Res. 41 (12) (2011) 1208–1223.
[2] P. Juilland, E. Gallucci, R. Flatt, K. Scrivener, Dissolution theory applied to the induction period in alite hydration, Cem. Concr. Res. 40 (6) (2010) 831–844.
[3] J.J. Thomas, J.J. Biernacki, J.W. Bullard, S. Bishnoi, J.S. Dolado, G.W. Scherer, A. Luttge, Modeling and simulation of cement hydration kinetics and microstructure development, Cem. Concr. Res. 41 (12) (2011) 1257–1278.
[4] T.C. Powers, Structure and physical properties of hardened portland cement paste, J. Am. Ceram. Soc. 41 (1) (1958) 1–6.
[5] P.K. Mehta, P.J.M. Monteiro, Concrete: microstructure, properties, and materials, 3rd ed. McGraw-Hill, New York, 2006.
[6] S. Mindess, J.F. Young, D. Darwin, Concrete, 2nd ed. Prentice Hall, Upper Saddle River, NJ, 2003.
[7] J.J. Beaudoin, Handbook of Analytical Techniques in Concrete Science and Technology, Noyes Publications, Park Ridge, NJ, 2000.
[8] S. Diamond, Mercury porosimetry - an inappropriate method for the measurement of pore size distributions in cement-based materials, Cem. Concr. Res. 30 (10) (2000) 1517–1525.
[9] I. Tekin, R. Birgul, H.Y. Aruntas, Determination of the effect of volcanic pumice replacement on macro void development for blended cement mortars by computerized tomography, Constr. Build. Mater. 35 (2012) 15–22.
[10] N. Narayanan, K. Ramamurthy, Structure and properties of aerated concrete: a review, Cem. Concr. Comp. 22 (5) (2000) 321–329.
[11] K.K. Aligizaki, Kalliopi K. Aligizaki, Pore Structure of Cement-based Materials: Testing, Interpretation and Requirements, CRC Press, 2005.
[12] S.W. Tang, X.H. Cai, Z. He, W. Zhou, H.Y. Shao, Z.J. Li, T. Wu, E. Chen, The review of pore structure evaluation in cementitious materials by electrical methods, Constr. Build. Mater. 117 (2016) 273–284.
[13] P. Lura, J. Couch, O.M. Jensen, J. Weiss, Early-age acoustic emission measurements in hydrating cement paste: evidence for cavitation during solidification due to self-desiccation, Cem. Concr. Res. 39 (10) (2009) 861–867.
[14] A. Bazzoni, M. Cantoni, K.L. Scrivener, Impact of annealing on the early hydration of tricalcium silicate, J. Am. Ceram. Soc. 97 (2) (2014) 584–591.
[15] K.O. Kjellsen, B. Lagerblad, Microstructure of tricalcium silicate and portland cement systems at middle periods of hydration-development of Hadley grains, Cem. Concr. Res. 37 (1) (2007) 13–20.
[16] D. Menetrier, I. Jawed, T.S. Sun, J. Skalny, Esca and sem studies on early C3s hydration, Cem. Concr. Res. 9 (4) (1979) 473–482.
[17] Q.N. Hu, M.T. Ley, J. Davis, J.C. Hanan, R. Frazier, Y.L. Zhang, 3D chemical segmentation of fly ash particles with X-ray computed tomography and electron probe microanalysis, Fuel 116 (2014) 229–236.
[18] L. Wang, B. Yang, A. Abraham, L. Qi, X.Y. Zhao, Z.X. Chen, Construction of dynamic three-dimensional microstructure for the hydration of cement using 3D image registration, Pattern. Anal. Applic. 17 (3) (2014) 655–665.
[19] E. Gallucci, K. Scrivener, A. Groso, M. Stampanoni, G. Margaritondo, 3D experimental investigation of the microstructure of cement pastes using synchrotron X-ray microtomography (mu CT), Cement Concrete Res 37 (3) (2007) 360–368.
[20] N. Bossa, P. Chaurand, J. Vicente, D. Borschneck, C. Levard, O. Aguerre-Chariol, J. Rose, Micro- and nano-X-ray computed-tomography: a step forward in the characterization of the pore network of a leached cement paste, Cem. Concr. Res. 67 (2015) 138–147.
[21] N. Burlion, D. Bernard, D. Chen, X-ray microtomography: application to microstructure analysis of a cementitious material during leaching process, Cem. Concr. Res. 36 (2) (2006) 346–357.
[22] Q. Hu, M. Aboustait, M.T. Ley, J.C. Hanan, V. Rose, R. Winarski, Combined three-dimensional structure and chemistry imaging with nanoscale resolution, Acta Mater. 77 (2014) 173–182.
[23] Q. Hu, M. Aboustait, T. Kim, M.T. Ley, J. Bullard, G. Scherer, J.C. Hanan, V. Rose, R. Winarski, J. Gelb, Direct measurements of 3d structure, chemistry and mass density during the induction period of C3s hydration, Cem. Concr. Res. 89 (2016) 14–26.
[24] M. Moradian, Q. Hu, M. Aboustait, M.T. Ley, J.C. Hanan, X. Xiao, V. Rose, R. Winarski, Multi-scale In-situ Observations of Structure and Chemistry Changes of Portland Cement Systems During Hydration, 2018 (Submitted).
[25] M.T. Ley, Q. Hu, M. Aboustait, T. Kim, M. Moradian, J. Hanan, V. Rose, R. Winarski, J. Gelb, Combining Nano X-ray Tomography and Nano X-ray Fluorescence to Create Time-dependent Three Dimensional Constitutive Maps, 2nd International Conference on Tomography of Materials and Structures(Quebec City, Canada) 2015.
[26] R.C.K. Wong, K.T. Chau, Estimation of air void and aggregate spatial distributions in concrete under uniaxial compression using computer tomography scanning, Cem. Concr. Res. 35 (8) (2005) 1566–1576.
[27] D.P. Bentz, S. Mizell, S. Satterfield, J. Devaney, W. George, P. Ketcham, J. Graham, J. Porterfield, D. Quenard, F. Vallee, H. Sallee, E. Boller, J. Baruchel, The visible cement data set, J. Res. Natl. Inst. Stand. 107 (2) (2002) 137–148.
[28] D.P. Bentz, D.A. Quenard, H.M. Kunzel, J. Baruchel, F. Peyrin, N.S. Martys, E.J. Garboczi, Microstructure and transport properties of porous building materials. II: three-dimensional X-ray tomographic studies, Mater. Struct. 33 (227) (2000) 147–153.
[29] D. Gastaldi, F. Canonico, L. Capelli, E. Boccaleri, M. Milanesio, L. Palin, G. Croce, F. Marone, K. Mader, M. Stampanoni, In situ tomographic investigation on the early hydration behaviors of cementing systems, Constr. Build. Mater. 29 (2012) 284–290.
[30] L. Helfen, E. Dehn, P. Mikulik, T. Baumbach, Three-dimensional imaging of cement microstructure evolution during hydration, Adv. Cem. Res. 17 (3) (2005) 103–111.
[31] K.Y. Kim, T.S. Yun, J. Choo, D.H. Kang, H.S. Shin, Determination of air-void parameters of hardened cement-based materials using X-ray computed tomography, Constr. Build. Mater. 37 (2012) 93–101.
[32] M.A.B. Promentilla, T. Sugiyama, T. Hitomi, N. Takeda, Quantification of tortuosity in hardened cement pastes using synchrotron-based X-ray computed microtomography, Cem. Concr. Res. 39 (6) (2009) 548–557.
[33] P.M. Rao, J.T. Rhea, R.A. Novelline, A.A. Mostafavi, C.J. McCabe, Effect of computed tomography of the appendix on treatment of patients and use of hospital resources, New Engl. J. Med. 338 (3) (1998) 141–146.

[34] W.C. Scarfe, A.G. Farman, P. Sukovic, Clinical applications of cone-beam computed tomography in dental practice, J. Can. Dent. Assoc. 72 (1) (2006) 75–80.
[35] P. Trtik, A. Diaz, M. Guizar-Sicairos, A. Menzel, O. Bunk, Density mapping of hardened cement paste using ptychographic X-ray computed tomography, Cem. Concr. Compos. 36 (2013) 71–77.
[36] M. Parisatto, M.C. Dalconi, L. Valentini, G. Artioli, A. Rack, R. Tucoulou, G. Cruciani, G. Ferrari, Examining microstructural evolution of portland cements by in-situ synchrotron micro-tomography, J. Mater. Sci. 50 (4) (2015) 1805–1817.
[37] J.J. Williams, Z. Flom, A.A. Amell, N. Chawla, X. Xiao, F. De Carlo, Damage evolution in SiC particle reinforced Al alloy matrix composites by X-ray synchrotron tomography, Acta Mater. 58 (18) (2010) 6194–6205.
[38] X.D. Zhang, C.J. Xia, X.H. Xiao, Y.J. Wang, Fast synchrotron X-ray tomography study of the packing structures of rods with different aspect ratios, Chin. Phys B 23 (4) (2014).
[39] P.W. Brown, E. Franz, G. Frohnsdorff, H.F.W. Taylor, Analyses of the aqueous phase during early C3s hydration, Cem. Concr. Compos. 14 (2) (1984) 257–262.
[40] J.F. Young, H.S. Tong, R.L. Berger, Compositions of solutions in contact with hydrating tricalcium silicate pastes, J. Am. Ceram. Soc. 60 (5–6) (1977) 193–198.
[41] Z.Q. Wu, J.F. Young, Formation of calcium hydroxide from aqueous suspensions of tricalcium silicate, J. Am. Ceram. Soc. 67 (1) (1984) 48–51.
[42] J.J. Chen, J.J. Thomas, H.F.W. Taylor, H.M. Jennings, Solubility and structure of calcium silicate hydrate, Cem. Concr. Compos. 34 (9) (2004) 1499–1519.
[43] D. Damidot, A. Nonat, P. Barret, Kinetics of tricalcium silicate hydration in diluted suspensions by microcalorimetric measurements, J. Am. Ceram. Soc. 73 (11) (1990) 3319–3322.
[44] F. Chalencon, L. Orgeas, P.J.J. Dumont, G. Foray, J.Y. Cavaille, E. Maire, S.R. du Roscoat, Lubricated compression and X-ray microtomography to analyse the rheology of a fibre-reinforced mortar, Rheol. Acta 49 (3) (2010) 221–235.
[45] F. De Carlo, P.B. Albee, Y.S. Chu, D.C. Mancini, B. Tieman, S.Y. Wang, High-throughput real-time X-ray microtomography at the advanced photon source, International Symposium on Optical Science and Technology, International Society for Optics and Photonics 2002, pp. 1–13.
[46] F. De Carlo, B. Tieman, High-throughput X-ray microtomography system at the advanced photon source beamline 2-BM, Optical Science and Technology, the SPIE 49th Annual Meeting, International Society for Optics and Photonics 2004, pp. 644–651.
[47] N.D. Parab, B. Claus, M.C. Hudspeth, J.T. Black, A. Mondal, J.Z. Sun, K. Fezzaa, X.H. Xiao, S.N. Luo, W.N. Chen, Experimental assessment of fracture of individual sand particles at different loading rates, Int. J. Impact Eng. 68 (2014) 8–14.
[48] J. Pourchez, B. Ruot, J. Debayle, E. Pourchez, P. Grosseau, Some aspects of cellulose ethers influence on water transport and porous structure of cement-based materials, Cem. Concr. Res. 40 (2) (2010) 242–252.
[49] J. Adrien, S. Meille, S. Tadier, E. Maire, L. Sasaki, In-situ X-ray tomographic monitoring of gypsum plaster setting, Cem. Concr. Res. 82 (2016) 107–116.
[50] J.W. Bullard, B. Lothenbach, P.E. Stutzman, K.A. Snyder, Coupling thermodynamics and digital image models to simulate hydration and microstructure development of portland cement pastes, J. Mater. Res. 26 (4) (2011) 609–622.
[51] W.A. Gerth, Effects of dissolved electrolytes on the solubility and partial molar volume of helium in water from 50 to 400 atmospheres at 25-degrees-C, J. Solut. Chem. 12 (9) (1983) 655–669.
[52] S.S. Todd, Low-temperature heat capacities and entropies at 298.16-degrees-K of crystalline calcium orthosilicate, zinc orthosilicate and tricalcium silicate, J. Am. Chem. Soc. 73 (7) (1951) 3277–3278.
[53] J. Zhang, E.A. Weissinger, S. Peethamparan, G.W. Scherer, Early hydration and setting of oil well cement, Cem. Concr. Res. 40 (7) (2010) 1023–1033.
[54] S. Peethamparan, E. Weissinger, J. Vocaturo, J. Zhang, G. Scherer, Monitoring Chemical Shrinkage Using Pressure Sensors, 270, ACI Special Publication, 2010 77–88.
[55] F. Fusseis, X. Xiao, C. Schrank, F. De Carlo, A brief guide to synchrotron radiation-based microtomography in (structural) geology and rock mechanics, J. Struct. Geol. 65 (2014) 1–16.
[56] J.H. Hubbell, Photon mass attenuation and energy-absorption coefficients from 1 Kev to 20 Mev, Int. J. Appl. Radiat. Isot. 33 (11) (1982) 1269–1290.
[57] D.R.K. Brownrigg, The weighted median filter, Commun. ACM 27 (8) (1984) 807–818.
[58] Z. Wang, D. Zhang, Progressive switching median filter for the removal of impulse noise from highly corrupted images, IEEE T Circuits-Ii 46 (1) (1999) 78–80.
[59] F.R. Brushett, L. Trahey, X.H. Xiao, J.T. Vaughey, Full-field synchrotron tomography of nongraphitic foam and laminate anodes for lithium-ion batteries, ACS Appl. Mater. Interfaces 6 (6) (2014) 4524–4534.
[60] C.W. Chung, P. Suraneni, J.S. Popovics, L.J. Struble, W.J. Weiss, Application of ultrasonic P-wave reflection to measure development of early-age cement-paste properties, Mater. Struct. 46 (6) (2013) 987–997.
[61] C.J.J. Fox, On the coefficients of absorption of nitrogen and oxygen in distilled water and seawater, and of atmospheric carbonic acid in sea-water, T Faraday Soc. 5 (1/2) (1909) 0068–0086.
[62] M.N. Kutty, Site Selection for Aquaculture: Chemical Features of Water, Food and Agriculture Organization (FAO), 1987.
[63] L.K. Wang, N.K. Shammas, W.A. Selke, D.B. Aulenbach, Gas dissolution, release, and bubble formation in flotation systems, Flotation Technology, Humana Press 2010, pp. 49–83.
[64] G.C. Whipple, M.C. Whipple, Solubility of oxygen in sea water, J. Am. Chem. Soc. 33 (1911) 362–365.
[65] R. Battino, T.R. Rettich, T. Tominaga, The solubility of oxygen and ozone in liquids, J. Phys. Chem. Ref. Data 12 (2) (1983) 163–178.
[66] M.M. Benjamin, Water Chemistry, McGraw-Hill, Boston, 2002.
[67] J.W. Bullard, R.J. Flatt, New insights into the effect of calcium hydroxide precipitation on the kinetics of tricalcium silicate hydration, J. Am. Ceram. Soc. 93 (7) (2010) 1894–1903.
[68] J.B. Ings, P.W. Brown, G. Frohnsdorff, Early hydration of large single-crystals of tricalcium silicate, Cem. Concr. Res. 13 (6) (1983) 843–848.
[69] G. Marrucci, L. Nicodemo, Coalescence of gas bubbles in aqueous solutions of inorganic electrolytes, Chem. Eng. Sci. 22 (9) (1967) 1257.
[70] Sa Zieminsk, M.M. Caron, Rb Blackmor, Behavior of air bubbles in dilute aqueous solutions, Ind. Eng. Chem. Fundam. 6 (2) (1967) 233.
[71] V.S.J. Craig, B.W. Ninham, R.M. Pashley, Effect of electrolytes on bubble coalescence, Nature 364 (6435) (1993) 317–319.
[72] P.K. Weissenborn, R.J. Pugh, Surface tension of aqueous solutions of electrolytes: relationship with ion hydration, oxygen solubility, and bubble coalescence, J. Colloid Interface Sci. 184 (2) (1996) 550–563.
[73] V.S.J. Craig, B.W. Ninham, R.M. Pashley, Study of the long-range hydrophobic attraction in concentrated salt solutions and its implications for electrostatic models, Langmuir 14 (12) (1998) 3326–3332.
[74] C.L. Henry, C.N. Dalton, L. Scruton, V.S.J. Craig, Ion-specific coalescence of bubbles in mixed electrolyte solutions, J. Phys. Chem. C 111 (2) (2007) 1015–1023.
[75] X.F. Pang, Water: Molecular Structure and Properties, World Scientific, 2014.
[76] M. Firouzi, T. Howes, A.V. Nguyen, A quantitative review of the transition salt concentration for inhibiting bubble coalescence, Adv. Colloid. Interf. 222 (2015) 305–318.
[77] K.A. Seeler, Fluid, electrical, and thermal systems, System Dynamics, Springer, New York, 2014.
[78] L.K. Wang, Flotation Technology, Humana, New York, 2010.
[79] P. Juilland, A. Kumar, E. Gallucci, R.J. Flatt, K.L. Scrivener, Effect of mixing on the early hydration of alite and OPC systems, Cem. Concr. Res. 42 (9) (2012) 1175–1188.
[80] X.S. Wei, Z.J. Li, Early hydration process of portland cement paste by electrical measurement, J. Mater. Civ. Eng. 18 (1) (2006) 99–105.
[81] A.L. Kelzenberg, S.L. Tracy, B.J. Christiansen, J.J. Thomas, M.E. Clarage, S. Hodson, H.M. Jennings, Chemistry of the aqueous phase of ordinary portland cement pastes at early reaction times, J. Am. Ceram. Soc. 81 (9) (1998) 2349–2359.
[82] L. Nicoleau, A. Nonat, D. Perrey, The di- and tricalcium silicate dissolutions, Cem. Concr. Res. 47 (2013) 14–30.
[83] P.W. Voorhees, The theory of Ostwald ripening, J. Stat. Phys. 38 (1–2) (1985) 231–252.
[84] V.S.J. Craig, Bubble coalescence and specific-ion effects, Curr. Opin. Colloid Interface 9 (1–2) (2004) 178–184.
[85] V.S.J. Craig, B.W. Ninham, R.M. Pashley, The effect of electrolytes on bubble coalescence in water, J. Phys. Chem.-Us 97 (39) (1993) 10192–10197.
[86] C.L. Henry, V.S.J. Craig, The link between ion specific bubble coalescence and Hofmeister effects is the partitioning of ions within the interface, Langmuir 26 (9) (2010) 6478–6483.